Extensions of Leading-Edge Modulated One-Cycle Control for Totem-Pole Bridgeless Rectifiers

Guilherme da Silva Fischer, Cassiano Rech, *Senior Member, IEEE*, and Yales Rômulo de Novaes, *Member, IEEE*

***Abstract*—Totem-Pole Bridgeless Rectifier (TPBR) is a promising power circuit topology for power factor correction, but low-cost input current sensing is a challenge in this topology that needs to be solved for its adoption in cost-sensitive applications. This article presents two new extensions to leading-edge modulated one-cycle control (LEM-OCC) that can achieve stable control of the TPBR using a shunt resistor connected to the low side of the output voltage for current sensing. Besides that, the proposed extensions also improves the performance of LEM-OCC, where one of them shows a reduction of 60% of the input current total harmonic distortion (THD) at light load and high input voltage, while the other shows a reduction of 45% of the input current THD. The higher performance extension requires a digital controller, but the second extension can be implemented with analog circuits. A 300-W prototype is used to validate the control equations and stability analysis.**

***Index Terms*—AC–DC power converters, current control, one-cycle control (OCC), power factor correction (PFC), rectifiers.**

I. Introduction

In POWER factor correction (PFC) applications, bridgeless rectifiers can achieve higher efficiency than the boost converter with diode bridge by decreasing conduction losses. At a first moment, totem-pole bridgeless rectifiers (TPBR) [1], as shown in Fig. 1, were limited by switching losses caused by reverse recovery of MOSFETs body diodes [2], limiting practical implementations to discontinuous conduction mode (DCM). On the other hand, high-performance silicon IGBT [3] and the advent of wide bandgap semiconductors, especially silicon carbide and gallium nitride (GaN), have brought the TPBR to the spotlight. Some GaN applications are achieving efficiencies higher than 99% by combining low conduction losses of the topology with low switching losses of these new devices [3]–[5].

Manuscript received October 25, 2018; revised February 23, 2019, May 13, 2019, and August 17, 2019; accepted October 2, 2019. Date of publication October 9, 2019; date of current version February 11, 2020. This article was supported by Research and Innovation Support Foundation of Santa Catarina State, *National Academic Cooperation Program* from *Coordination for the Improvement of Higher Education Personnel*—CAPES, Brazil. Recommended for publication by Associate Editor Prof. Q. Li. *(Corresponding author: Guilherme da Silva Fischer.)*

G. S. Fischer and Y. R. de Novaes are with the Department of Electrical Engineering, Santa Catarina State University, Joinville 89219-710, Brazil (e-mail: guilherme.silva.fischer@gmail.com; yales.novaes@udesc.br).

C. Rech is with the Power Electronics and Control Research Group, Federal University of Santa Maria, Santa Maria 97105-900, Brazil (e-mail: rech.cassiano@gmail.com).

Color versions of one or more of the figures in this article are available online at http://ieeexplore.ieee.org.

Digital Object Identifier 10.1109/TPEL.2019.2946570

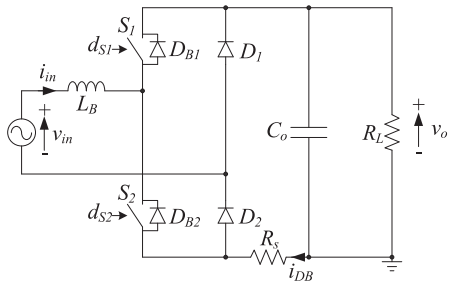

Fig. 1. Totem-pole bridgeless rectifier.

To obtain high power factor, the input current i_{in}, in Fig. 1 needs to be controlled. In addition, low-cost sensing and control are requirements for the TPBR to receive acceptance for mass-market applications (i.e., cost sensitive). On the other hand, sensing the input current is not too simple in the TPBR because the ac supply is not directly connected to the output reference. As an attempt to overcome this problem, in [4], the control circuit reference is changed to the input inductor and a shunt resistor is used for current sensing. This strategy requires an isolated dc–dc power supply and isolated gate drivers, increasing cost. Furthermore, among other more complex solutions, changing the control circuit ground complicates control of a downstream converter, such as an inverter, due to different reference levels, requiring isolated sensors for the inverter control or a second set of control circuits.

The use of a Hall effect sensor with suitable bandwidth for measuring the input current is cost prohibitive for mass-market applications; therefore, a control strategy compatible with a simple sensing strategy is required. One-cycle control (OCC) [6], [7] can be used in ac–dc active PFC (APFC) applications, and it is possible to use simple sensors. When applied to the TPBR, trailing-edge modulated OCC (TEM-OCC) requires two current transformers (CTs), while leading-edge modulated OCC (LEM-OCC) requires only a shunt resistor connected to the output ground, i.e., the low-side shunt resistor (LSSR) R_s shown in Fig. 1. LEM-OCC presents significantly worse stability issues and distortion of the controlled signal than TEM-OCC, severely limiting its applications.

The original implementation of TEM-OCC still presents some stability issues and distortion of the controlled signal, but they are not as severe as LEM-OCC. Due to this fact, TEM-OCC has been used successfully in applications such as ac–dc converters [7]–[9], dc–ac converters [10], [11],

multiple input converters [12], and second harmonic current compensation in ac–dc–ac converters [13]. Moreover, solutions have been proposed over time to further improve stability and reduce distortion of TEM-OCC [8]–[10], [13]–[16], including modifications in the control law and the addition of a fictitious current to the sensed current, but these have not aimed to decrease the current sensing requirements of TEM-OCC. These solutions can be applied to LEM-OCC to take advantage of the simpler current sensor, but are not enough to achieve stability and low total harmonic distortion (THD) at the same time, especially at light load when the converter switches to DCM. OCC using combined leading-edge and trailing-edge modulations [17]–[19] can eliminate the current distortion, but does not allow DCM operation. It requires sensing the input current during the whole switching cycle, which, in turn, requires a Hall effect sensor.

To give context to the analysis, the use of a TPBR in an inverter driven refrigerator is considered. In this application, an inverter drives the brushless dc motor that powers the compressor. High total system efficiency is required, which makes the TPBR interesting as the APFC converter. It is also a cost-sensitive application, which makes LEM-OCC interesting so that the APFC converter and the output inverter can operate in the same ground reference while using simple sensors. Household refrigerators consume around its rated power while cooling down its temperature. This process is called pull-down, which defines the maximum required power of the power electronics stage. After the pull-down procedure, the energy consumption decreases to less than 40%. In the near future, depending on the refrigerator thermal isolation and added electronic functionality, its power consumption may reduce even more. Therefore, the light load stability and THD of LEM-OCC need to be improved to make this application feasible.

Therefore, this article presents an analysis of LEM-OCC and new extensions that add a fictitious current to the sensed current to improve both its stability and input current distortion. The goal is to make LEM-OCC a viable alternative to TEM-OCC and other existing control strategies, while keeping the advantage of using a single shunt resistor for current sensing.

This article is organized as follows. Section II reviews different control strategies that can be applied to TPBR, and shows how LEM-OCC and TEM-OCC are positioned against other control strategies. Section III presents how the use of a fictitious current affects LEM-OCC. Section IV presents how this fictitious current allows implementation of three different LEM-OCC extensions, one based on literature that improves only stability, and two new extensions that improve both input current distortion and stability. The first of these new extensions uses a digital signal processor (DSP) to achieve higher performance (called LEM-OCC-SD because it improves both stability and distortion). The second proposed extension can be implemented using analog hardware (LEM-OCC-SDS, with an additional S for simplified). Section V includes experimental results of a TPBR with wide input power and voltage ranges. Section VI concludes this article.

II. Control Strategies for TPBR

Table I presents some APFC control strategies and their required input current and input voltage sensors. The need of a DSP for dealing with more complicate calculations is also identified. All these strategies use ground-referenced circuits to avoid using isolated auxiliary power supplies. LEM-OCC-SD and LEM-OCC-SDS are the two new extensions proposed in this article. LEM-OCC-SD requires input voltage waveform sensing and a DSP, which were not required by the original LEM-OCC. LEM-OCC-SDS has the same requirements as LEM-OCC. These proposed strategies are discussed in detail in Section IV. For the TPBR, at least an input voltage polarity detector is required as switches S_1 and S_2 cannot be driven by the same pulsewidth modulation (PWM) signal [2]. However, some control strategies also require the input voltage waveform to be sensed.

TABLE I
Possible Control Strategies for TPBR

Control Strategy	Requires a DSP	Current Sensor	Input Voltage Sensor
Average Analog (A-A) [20]	No	Hall or 3xCT	Waveform
Digital-Average (D-A) [21]	Yes	2xCT	Polarity
TEM-OCC [7], [22]	No	2xCT	Polarity
Digital-Peak Current (D-PC) [3]	Yes	LSSR	Polarity
LEM-OCC [7]	No	LSSR	Polarity
LEM-OCC-SD	Yes	LSSR	Waveform
LEM-OCC-SDS	No	LSSR	Polarity

Average analog (A-A) control requires sensing the input current during the whole switching period, allowing the control of average values and resulting in satisfactory THD under light load operation. The input current sensing for analog control can be implemented either by using a Hall effect sensor or by reconstructing the input current with three CTs sensing switched currents. A-A control also requires sensing the input voltage waveform to generate the current reference.

Digital-Average (D-A) control using rising edge sampling [23] samples the input current during switch ON time. This sensing requirement can be implemented with one CT for each switch. In D-A control, during CCM operation the input current sample is equal to the average input current and the controller can achieve low input current THD. However, this is not true during DCM operation, resulting in increased input current THD at light load. D-A control does not require sensing the input voltage waveform as the DSP can generate a sine wave internally, synchronized to the polarity detection.

TEM-OCC [7], [22] controls the OFF-time of the switches in a comparison involving the input current and the output of an integrator. This results in the peak input current being controlled, causing higher input current THD than A-A control and similar performance to D-A control. This strategy requires sensing the input current only during switch ON-time and has already been applied to bridgeless rectifiers using two CTs for current sensing [24]. TEM-OCC also has the advantage of not requiring sensing the input voltage waveform and it does not require a DSP.

Digital-peak current (D-PC) [3] control and LEM-OCC [7] requires to sense the current in the i_{DB} path using an LSSR. When diodes D_{B1} or D_{B2} are ON, their current pass through

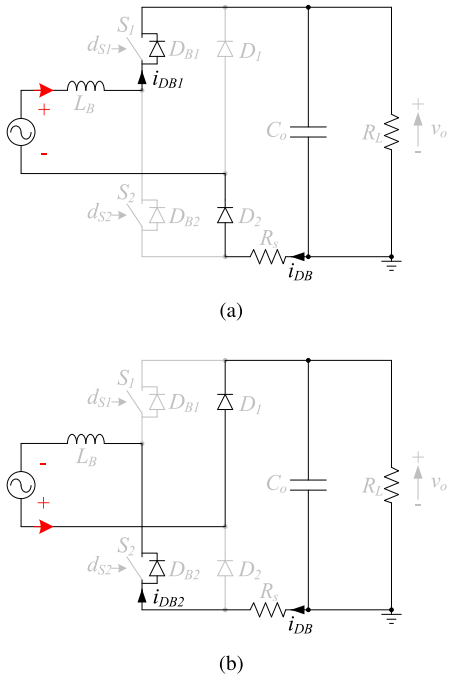

Fig. 2. Shared current path of diodes D_{B1} and D_{B2}. (a) Diode D_{B1} conducts for $i_{in} > 0$. (b) Diode D_{B2} conducts for $i_{in} < 0$.

the same path i_{DB}, as presented in Fig. 2. For positive i_{in}, D_{B1} conducts when the switches are OFF, as shown in Fig. 2(a). For negative i_{in}, D_{B2} conducts when the switches are OFF, as shown in Fig. 2(b). D-PC control uses the i_{DB} current sensing to sample the peak of the inductor current after the diodes turn ON. A small delay (blanking time) is necessary due to the settling time of the sensor. Since the peak current of the inductor is sampled, when current ripple is high, the resulting THD is also high. A DSP could generate the current reference internally to avoid using an input voltage waveform sensor.

Similar to TEM-OCC, LEM-OCC [7] achieves control of the input current by using a comparison involving the input current and the output of an integrator. However, LEM-OCC controls the switch ON-time of the switches, which results in controlling the valley of the input current in a switching cycle to be proportional to the input voltage. The advantage of LEM-OCC is that it requires a single LSSR for current sensing instead of the two CTs required by TEM-OCC. However, LEM-OCC presents both high THD and stability problems at light load when operating with low voltage gain. This limits its use in applications like household refrigerators and, in practice, it cannot compete with TEM-OCC.

For comparison purposes, the parameters of an ac–dc converter used as the input stage of an inverter driven refrigerator are shown in Table II. This converter is simulated using the control strategies presented in Table I, with output power varied from the minimum output power $P_o^{\min}$ to the maximum output power $P_o^{\max}$ and the input voltage v_{in} fixed at its maximum value of $V_{\text{in}}^{\text{rms,max}}$. No power losses or parasitic elements are considered in the simulation. In the simulations, the controller for A-A control has 8 kHz bandwidth with 60° phase margin. The digital

TABLE II
PARAMETERS OF A TPBR FOR AN INVERTER REFRIGERATOR

Parameter	Description	Value
$V_{in}^{rms,max}$	Maximum input voltage	250 V
f_r	Line frequency	60 Hz
L_B	Boost Inductance	2.4 mH
P_o^{min}	Minimum output power	25 W
P_o^{max}	Maximum output power	300 W
V_o	Output voltage	380 V
C_o	Output Capacitance	270 μF
f_s	Switching frequency	64.8 kHz

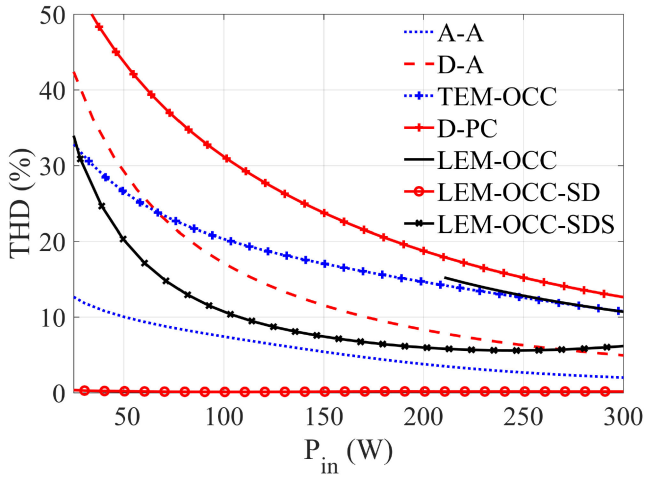

Fig. 3. Input current THD as a function of input power for different control strategies. $V_{\text{in}}^{\text{rms}} = 250$ V. $R_f = 361\,\Omega$ for LEM-OCC-SD. $a = 0.978$ and $b = 0.0028$ for LEM-OCC-SDS.

controllers for D-A and D-PC are obtained by discretization of the analog controller. The resulting THD (calculated up to the 40th line frequency harmonic) as a function of the input power P_{in} is shown in Fig. 3. As expected, A-A control has low THD, while D-A control achieves good performance when the input power is high. D-A control has worse performance than TEM-OCC at lower power levels. D-PC control has the highest THD and LEM-OCC is not stable during the whole operating range of the converter.

The extensions proposed in this article are shown in Fig. 3 for completeness. Theoretically (numerical simulation), LEM-OCC-SD can achieve zero THD while using a simple current sensor. However, this improved performance requires a DSP and input voltage waveform sensing. LEM-OCC-SDS has performance similar to TEM-OCC, both require only analog circuits, but LEM-OCC-SDS has the lower current sensing requirements.

III. LEM-OCC WITH FICTITIOUS CURRENT

First, a brief review of LEM-OCC applied to the TPBR is presented. In the TPBR only, one switch operates during each half of the input voltage cycle. The other switch can be kept open or receive the complementary driving signal. Therefore, the command signal with duty ratio d is applied to the switch S_2 for positive v_{in}, and to the switch S_1 for negative v_{in}.

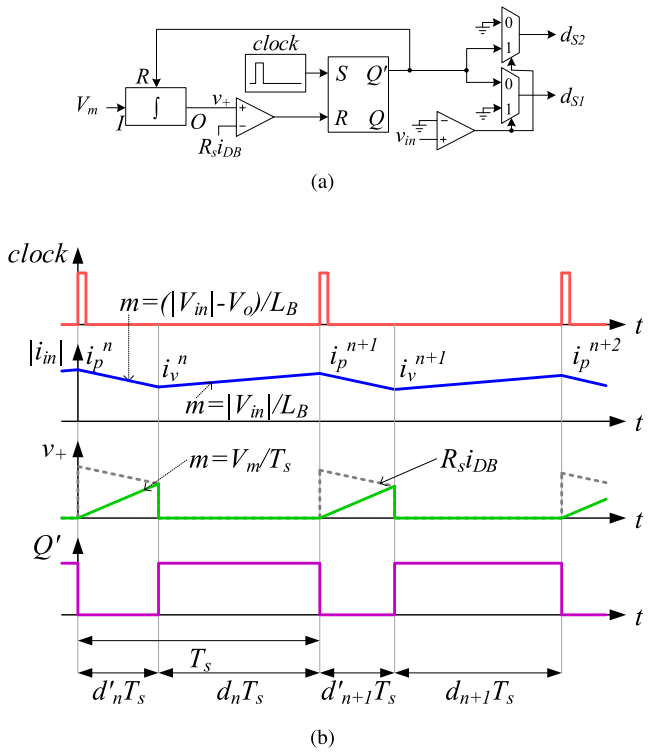

Fig. 4. LEM-OCC. (a) Circuit for the TPBR. (b) Waveforms [7].

The resulting steady-state voltage gain $M(D)$ is given by

$$M(D) = \frac{V_o}{|V_{\text{in}}|} = \frac{1}{1-D} \tag{1}$$

where v_o is the output voltage and uppercase letters represent constant or steady-state values.

To achieve PFC, the input current of a rectifier should be controlled to emulate a resistance R_e, that is

$$\langle i_{\text{in}} \rangle = \frac{v_{\text{in}}}{R_e} \tag{2}$$

with lowercase letters representing a time-variant variable, and the angular bracket the average value in a switching period.

In general, this objective can be accomplished with the control law [7]

$$R_s \langle i_{\text{in}} \rangle = \frac{V_m}{M(D)} = \frac{v_{\text{in}} V_m}{V_o} \tag{3}$$

where V_m is the modulating voltage. Implementation of this control law can be accomplished with LEM-OCC. By rearranging (3), one can see that the effective emulated resistance is controlled by adjusting the amplitude of V_m

$$R_e = \frac{|v_{\text{in}}|}{|\langle i_{\text{in}} \rangle|} = \frac{R_s V_o}{V_m}. \tag{4}$$

The LEM-OCC block diagram for application in the TPBR is shown in Fig. 4(a) and it is obtained from the general pulsewidth modulator in [7]. The analysis presented in [7] for the boost converter with diode bridge is valid for the TPBR by using absolute values of inductor current and input voltage. In leading-edge modulation, Q' is the command signal. A digital multiplexer is used to select the switch to receive the command signal. The current of both boost diodes is sensed in the i_{DB} path. The sensor gain is represented by sensing resistance R_s as illustrated in Fig. 1.

Waveforms of LEM-OCC are presented in Fig. 4(b), considering constant values for input and output voltages. Variables i_p^n and i_v^n represent the peak and valley of the input current, d_n and $d'_n = 1 - d_n$ are the duty ratio and complementary duty ratio, index n represents the nth switching cycle, m is the inclination of a given curve, L_B is the boost inductance, and T_s is the switching period. The turn-OFF instant of Q' is synchronized to the clock rising edge, while the turn-ON instant is variable, which leads to the name *leading-edge modulation*. When Q' is OFF, if the ramp v_+, output of the OCC integrator, with inclination V_m/T_s, and the sensed current signal $R_s i_{DB}$, with inclination $R_s(|V_{\text{in}}| - V_o)/L_B$, do not cross before the next clock rising-edge, the command signal skips a switching cycle. The result of skipping a switching cycle is the presence of subharmonic oscillation in the input current. Therefore, the inclination of signals v_+ and $R_s i_{DB}$ are directly related to the instability problems of LEM-OCC. The stability criteria of LEM-OCC is

$$\frac{L_B f_s}{R_e} + D > \frac{1}{2} \tag{5}$$

where $f_s = 1/T_s$ is the switching frequency and the duty ratio D is calculated from the TPBR steady-state voltage gain in (1) [7]. Equation (5) imposes significant design restrictions for guaranteeing controller stability, as it requires limiting the input voltage peak to half the output voltage, or the converter to operate with a minimum input power (i.e., with a maximum emulated resistance R_e).

The minimum input power required for LEM-OCC, when operating with input voltage peak close to the output voltage, represents a large percentage of the rated input power. This does not satisfy some application requirements like household refrigerators due to their low power consumption after the pull-down process has finished. As an example, at maximum input voltage, the converter from Table II requires a minimum input power of 151 W (≈50% of $P_o^{\max}$). In fact, the minimum input power where stability is kept is even higher, as (5) is derived considering the small input current ripple approximation.

A. Stability of LEM-OCC With Fictitious Current in CCM

The approach from [9], [15], and [16] that adds a fictitious current to the sensed signal can be applied to LEM-OCC controlling the TPBR by using the circuit in Fig. 5. However, in [9], [15], and [16], the fictitious current, i_f, has the same waveform as the input voltage and is defined as

$$i_f = \frac{|v_{\text{in}}|}{R_f} \tag{6}$$

where R_f is the fictitious resistance. In the new extensions presented in this article, the fictitious current can have any waveform. This allows improving both stability and input current THD. A digital controller can be used to generate the fictitious

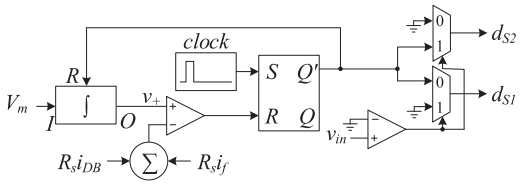

Fig. 5. LEM-OCC circuit with fictitious current for the TPBR.

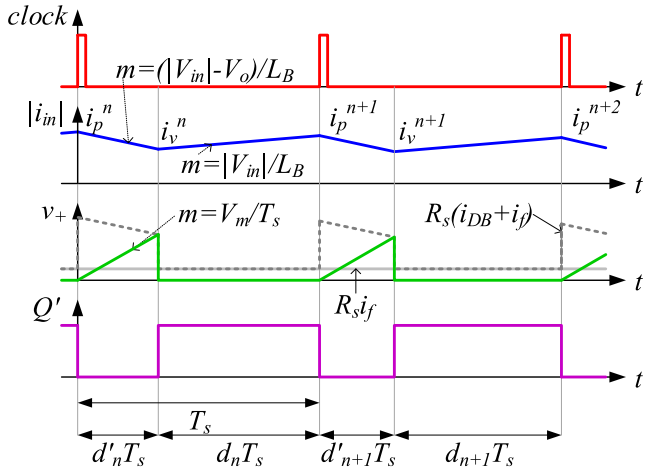

Fig. 6. Waveforms of LEM-OCC with fictitious current, during CCM operation.

current with complex waveforms. Alternatively, analog circuits can generate the fictitious current with simpler waveforms.

The methodology presented in [7] is used here to analyze the stability of LEM-OCC with fictitious current of any waveform. Fig. 6 presents the waveforms when operating in CCM. It is considered that $v_{\text{in}} \approx V_{\text{in}}$ for a few switching cycles. The flip-flop in the control circuit of Fig. 5 resets when

$$\left(i_p^n + i_f + \frac{|V_{\text{in}}| - V_o}{L_B} t\right) R_s = \frac{V_m}{T_s} t, (0 \le t \le T_s) \tag{7}$$

where time $t = d'_n T_s = (1 - d_n)T_s$, so (7) is reorganized as

$$d'_n = \left(i_p^n + i_f\right) \left(\frac{V_m}{R_s} + \frac{V_o - |V_{\text{in}}|}{L_B f_s}\right)^{-1}. \tag{8}$$

The peak current in the switching cycle $n+1$ is found from the waveforms and it can be given by

$$i_p^{n+1} = i_p^n + \frac{|V_{\text{in}}|}{L_B} T_s - \frac{V_o}{L_B} d'_n T_s \tag{9}$$

which is combined with (8), resulting in

$$i_p^{n+1} = \frac{|V_{\text{in}}|}{L_B} T_s + (K_s - 1) i_f + i_p^n K_s \tag{10}$$

where

$$K_s = 1 - \left(\frac{L_B f_s V_m}{R_s V_o} + \frac{V_o - |V_{\text{in}}|}{V_o}\right)^{-1}. \tag{11}$$

To simplify the stability analysis, it is considered that i_f is not a function of the input current, so that (10) has the form $a^{n+1} = K_0 + K_s \cdot a^n$, and will converge to a finite value only when [25]

$$|K_s| < 1. \tag{12}$$

Equations (11) and (12) show that the fictitious current does not directly affect the stability of current control in LEM-OCC, as it is only dependent on the modulating voltage V_m, input and output voltages, and converter parameters. This is valid for any format of fictitious current that does not use samples of the input current. The stability analysis is also valid during input and output voltage transients, as long as they can be approximated as constant values during a switching cycle. However, the fictitious current does affect the steady-state value of input current. This means that the fictitious current can be used to decrease the input current while keeping V_m high to satisfy (12).

B. Average Input Current of LEM-OCC With Fictitious Current in CCM

The average input current in CCM is found by analyzing the waveforms in Fig. 6 and considering that the converter reaches steady state. The steady-state peak inductor current, I_p, is calculated by combining (1), (8) and the steady-state approximation $d = D$, yielding

$$I_p = \frac{|V_{\text{in}}|}{V_o} \left(\frac{V_m}{R_s} + \frac{V_o - |V_{\text{in}}|}{L_B f_s}\right) - i_f. \tag{13}$$

The steady-state valley of the input current, I_v, is found from the waveforms in Fig. 6 and it is given by

$$I_v = I_p - \frac{V_o - |V_{\text{in}}|}{L_B} D' T_s = \frac{|V_{\text{in}}| V_m}{V_o R_s} - i_f. \tag{14}$$

Considering the approximations $v_{\text{in}} = V_{\text{in}}$ and $i_{\text{in}} = I_{\text{in}}$, the average input current is

$$|\langle i_{\text{in}} \rangle| = \frac{I_p + I_v}{2} = \frac{|v_{\text{in}}|}{V_o} \left(\frac{V_m}{R_s} + \frac{V_o - |v_{\text{in}}|}{2 L_B f_s}\right) - i_f. \tag{15}$$

It can be seen from (15) that i_f and V_m can affect the average input current of the converter. Therefore, a suitable control law can satisfy both (2), to achieve low THD, and (12), to achieve stability.

C. Average Input Current of LEM-OCC Without Fictitious Current

The input current of LEM-OCC without the fictitious current can be analyzed by setting $i_f = 0$ in (14) and combining with (4), resulting in

$$I_v = \frac{|V_{\text{in}}|}{R_e} \tag{16}$$

which shows that the valley of the input current follows v_{in}/R_e in LEM-OCC. This causes high input current distortion if the current ripple is not small. Furthermore, as R_e gets higher, the valley of the input current gets closer to zero at the end of each switching cycle. Therefore, LEM-OCC without fictitious current will enter critical conduction mode (CRCM) when $V_m \to 0$

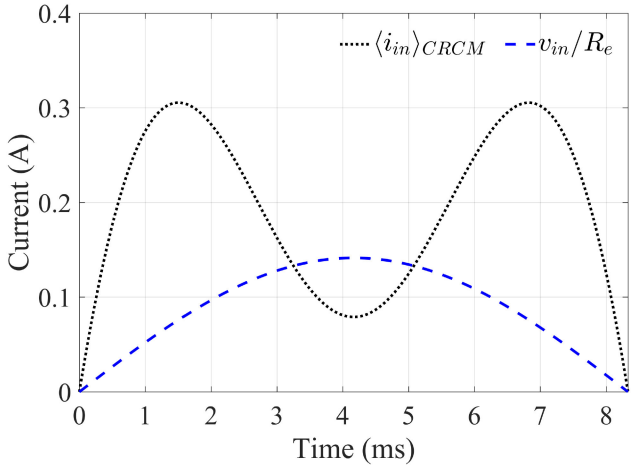

Fig. 7. LEM-OCC without fictitious current. Input current in CRCM mode and v_{in}/R_e for $V_{\text{in}}^{\text{rms}} = 250$ V, $R_e = 2500\,\Omega$.

($R_e = \infty$). This also implies that LEM-OCC without fictitious current cannot operate in DCM.

The average input current in CRCM, $|\langle i_{\text{in}}\rangle|_{\text{CRCM}}$, can be calculated by setting $i_f = 0$ and $V_m = 0$ ($R_e = \infty$) in (15), and it is given by

$$|\langle i_{\text{in}}\rangle|_{\text{CRCM}} = \frac{|v_{\text{in}}|}{V_o}\left(\frac{V_o - |v_{\text{in}}|}{2L_B f_s}\right). \tag{17}$$

In the TPBR, it is not possible to have input current with polarity different than the input voltage, and, therefore, the lowest average input current while operating in CCM occurs in the CRCM boundary. The average input current can only be lower than the one at CRCM by transitioning to DCM. Since LEM-OCC is limited to CRCM, there will be a minimum input current and, therefore, a minimum power consumption (MPC), even as $V_m \to 0$. The MPC can be calculated with help from (17). Output overvoltage will occur if the minimum load is lower than the MPC.

For instance, the parameters specified in Table II determine that stability and low THD should be achieved at light load (less than 10% of maximum output power), when only low-power auxiliary circuits of the refrigerator are operating. However, for the given converter parameters, during a line cycle with maximum input voltage, the MPC is 42 W. This MPC is higher than the minimum output power, representing a problem for output voltage control. Furthermore, it is usual that the converter will operate in DCM at light load [8]. It can be verified from Fig. 7 that if the converter cannot operate in DCM to decrease the input current, it cannot properly emulate a resistance whenever $v_{\text{in}}/R_e < |\langle i_{\text{in}}\rangle|_{\text{CRCM}}$ and will present input current distortion.

D. Stability of LEM-OCC With Fictitious Current in DCM

Fig. 8 presents the main waveforms of LEM-OCC with fictitious current operating in DCM. One can see from Fig. 8 that in DCM operation $|i_{\text{in}}|$ will reach zero before the switch turns ON, resulting in the flip-flop reset condition

$$V_m d'_n = R_s i_f. \tag{18}$$

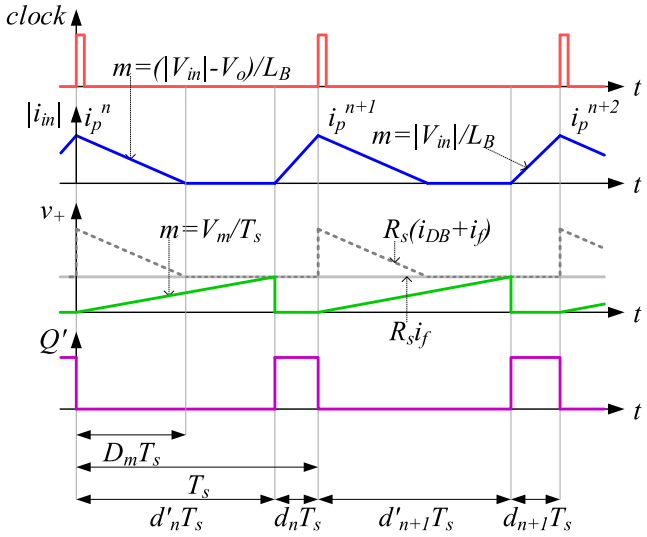

Fig. 8. Waveforms of LEM-OCC with fictitious current during DCM operation.

Therefore, the duty cycle in DCM is directly controlled by the fictitious current

$$d'_n = \frac{R_s i_f}{V_m}, 0 \le d' \le 1 \tag{19}$$

and the resulting peak input current in the $n+1$ cycle is

$$i_p^{n+1} = \left(1 - \frac{R_s i_f}{V_m}\right)\frac{|V_{\text{in}}|}{L_B f_s}. \tag{20}$$

Equation (20) also has the form $a^{n+1} = K_0 + K_s a^n$ and it is stable for $|K_s| < 1$. However, in this case, $K_s = 0$, and DCM operation is inherently stable. In this condition, the input current feedback is limited. Disturbances, such as switching delays, which keep the converter in DCM, will not be compensated by the controller, causing steady-state error, but disturbances that temporally bring the converter to CCM will result in controller action.

E. Average Input Current of LEM-OCC With Fictitious Current in DCM

The average input current in steady-state DCM, for the TPBR, is equivalent to the boost converter [26], and it is given by

$$|\langle I_{\text{in}}\rangle| = \frac{1}{2}\left(\frac{V_o\,|V_{\text{in}}|}{V_o - |V_{\text{in}}|}\right)\frac{D^2}{L_B f_s} \tag{21}$$

which is combined with (19) considering steady-state approximations, $d'_n = D'$, $v_{\text{in}} = V_{\text{in}}$ and $i_{\text{in}} = I_{\text{in}}$, yielding

$$|\langle i_{\text{in}}\rangle| = \frac{1}{2L_B f_s}\left(\frac{V_o\,|v_{\text{in}}|}{V_o - |v_{\text{in}}|}\right)\left(1 - \frac{R_s i_f}{V_m}\right)^2. \tag{22}$$

Similarly to the CCM operation, i_f and V_m can affect the average input current of the converter when operating in DCM.

IV. Extensions of the OCC Control Law

In this section, the control law (3) is modified to take advantage of the additional degree of freedom given by the fictitious

current. Three modifications are presented. The first is based on the modification presented in (6), where the fictitious current is proportional to the input voltage, resulting in LEM-OCC-S. This extension improves stability toward the lower power end but does not improve input current THD. A new extension of the control law is proposed to improve the input current THD at a wide input power range. To achieve this, the fictitious current is allowed to have any waveform so it can compensate the distortion in both CCM and DCM. The resulting controller is called LEM-OCC-SD and can achieve both stability and low input current THD. A simplification of the fictitious current calculated for LEM-OCC-SD results in LEM-OCC-SDS, which allows for implementation using only analog circuits.

The output voltage controller is designed considering that the relationship between input power and modulating voltage V_m is monotonically increasing, i.e., an increase in the modulating voltage V_m causes an increase in input power. This condition is satisfied by control laws presented in this section.

A. Leading-Edge Modulated One-Cycle Control-S

The fictitious current (6) [15] can be used to improve the stability of LEM-OCC, by changing the control law to

$$R_s\left(|\langle i_{\text{in}}\rangle| + i_f\right) = \frac{V_m\,|v_{\text{in}}|}{V_o} \tag{23}$$

and using the fictitious current (6), resulting in LEM-OCC-S.

Combining (2), (6), and (23) yields

$$R_{eq} = \frac{R_e R_f}{R_e + R_f} = \frac{R_s V_o}{V_m} \tag{24}$$

and the resulting stability criteria is found by combining (6), (11), (12), and (24)

$$\frac{L_B f_s}{R_{eq}} + D > \frac{1}{2} \tag{25}$$

which is similar to the stability criteria of LEM-OCC, except that it is now limited by the equivalent resistance R_{eq}. By using (25), a value of R_f can be calculated to guarantee stability down to no-load operation.

The average input current in a switching cycle is calculated by combining (6), (15), and (24)

$$|\langle i_{\text{in}}\rangle| = \frac{|v_{\text{in}}|}{R_e}\left(1 + \frac{V_o - |v_{\text{in}}|}{V_o}\frac{R_e}{2L_B f_s}\right). \tag{26}$$

Equation (26) shows that the average input current is always higher than the desired $|v_{\text{in}}|/R_e$, since $V_o \geq |v_{\text{in}}|$, and it is not affected by i_f. Therefore, with the control law (23), it is possible to achieve stability, but the resulting THD is the same as the one found in LEM-OCC. The converter can now operate in DCM solving the MPC issue.

B. Leading-Edge Modulated One-Cycle Control-SD

A second modification to the control law is necessary to reduce the current distortion and to improve stability. This extension is referenced here as LEM-OCC-SD. In this modification, a digital controller generates the fictitious current signal, which is not limited to be proportional to the input voltage as in [9], [15], and [16]. By removing these limitations, the fictitious current can improve both stability and the input current distortion in DCM and CCM. Two terms compose this new fictitious current, which is given by

$$i_f = i_f^s + i_f^e. \tag{27}$$

The first term, i_f^s, is the stability term and is defined as

$$i_f^s = \frac{|v_{\text{in}}|}{R_f} \tag{28}$$

and is based on [9], [15], and [16] to improve stability. Term i_f^e is the error term, used for compensating the input current error from LEM-OCC, in both CCM and DCM. Term i_f^e is an improvement to the proposed in [8] and [14], and can be computed using the control goal (2) to allow both DCM and CCM compensation.

The goal is still to emulate a resistance, but the input current is separated in two terms

$$|\langle i_{\text{in}}\rangle| = i_{\text{in}}^f + i_{\text{in}}^e \tag{29}$$

where i_{in}^e is the error in the input current present in LEM-OCC and $i_{\text{in}}^f = |v_{\text{in}}|/R_e$ is the term of the input current that emulates the desired input resistance. The control law proposed in [7] is extended to include the fictitious current from (27) and the separation from (29), resulting in

$$R_s\left(i_{\text{in}}^f + i_{\text{in}}^e + i_f^s + i_f^e\right) = \frac{V_m}{M(D)}. \tag{30}$$

Setting $i_f^e = -i_{\text{in}}^e$ to compensate the error in the input current and combining (1) and (30), results in

$$R_{\text{eq}} = \frac{R_e R_f}{R_e + R_f} = \frac{R_s V_o}{V_m} \tag{31}$$

which is the same as (24).

Combining (11), (12), and (31) yields another form for the stability criterion

$$\frac{L_B f_s}{R_{\text{eq}}} + D > \frac{1}{2} \tag{32}$$

which implies that R_f can be calculated to guarantee stability down to no-load operation.

1) Fictitious Current in Continuous Conduction Mode: To emulate a resistance with low distortion, (2) and (27) are combined with (15), yielding

$$i_f^e = \frac{|v_{\text{in}}|}{2L_B f_s V_o}(V_o - |v_{\text{in}}|). \tag{33}$$

The solution for i_f^e does not use samples of the input current, and, therefore, satisfies the assumption made to obtain (12). It also does not place restrictions on the value of R_f so both stability and input current compensation can be achieved independently in CCM. Furthermore, the compensation is dependent on the input inductance, and requires input and output voltage sensing.

2) Fictitious Current in DCM: The value for i_f during DCM operation is found by combining (2) and (31) with (22)

resulting on

$$i_f = \frac{V_m}{R_s}\left(1 - \sqrt{2L_B f_s \frac{V_o - |v_{\text{in}}|}{V_o}\left(\frac{V_m}{R_s V_o} - \frac{1}{R_f}\right)}\right) \quad (34)$$

which is dependent on the inductor value and requires computation of a square root.

In a DCM operation, i_f^e is not independent of R_f, and it cannot be separated from i_f^s. Therefore, i_f is calculated directly with (34). However, DCM operation is inherently stable and (34) places only the restriction that $R_f > 0$. This implies that R_f can be calculated to satisfy the CCM stability criterion without placing restrictions on stability or input current compensation in DCM.

The equations for computing the fictitious current in DCM and CCM are based on the same control law (30). Therefore, (34) includes R_f even though it is not necessary for stability in DCM. This keeps the relationship between V_m and R_e consistent during conduction mode transition. By doing so, the CCM and DCM equations of the fictitious current converge to the same value during CRCM while making the transition between conduction modes smooth.

Besides that, the stability criterion (11) is not directly dependent on the fictitious current, but on V_m, which is almost constant in a line cycle. Therefore, the stability is not compromised by errors in the fictitious current, caused by imperfect conduction mode transition, noise and offset in the analog circuits, or even an update rate of the fictitious current lower than the switching frequency. These errors should be small enough to not affect the average input current significantly and they would not affect the value of V_m. Additional stability margin can be added by further increasing R_f, and it does not compromise the THD improvement, as the only restriction from (33) and (34) is that $R_f > 0$.

Since equations for i_f are different for CCM and DCM, it is necessary to decide which equation should be used. Considering steady-state duty-ratio $d_n \to D$ in Fig. 8, the converter operates in DCM when

$$D + D_m < 1 \quad (35)$$

where demagnetizing-ratio D_m is found from the waveforms and it is given by

$$D_m = \frac{|V_{\text{in}}|}{V_o - |V_{\text{in}}|} D. \quad (36)$$

The duty-ratio in DCM is found by combining the desired input current (2) with (21)

$$D = \sqrt{\frac{2L_B f_s}{R_e}\frac{V_o - |V_{\text{in}}|}{V_o}}. \quad (37)$$

Combining (35), (36), and (37) results in

$$|v_{\text{in}}| < \frac{2L_B f_s V_o}{R_f} + V_o - \frac{2L_B f_s V_m}{R_s} \quad (38)$$

which is true when the converter has to operate in DCM to satisfy (2), and it can be used by a DSP to select the proper equation to calculate i_f.

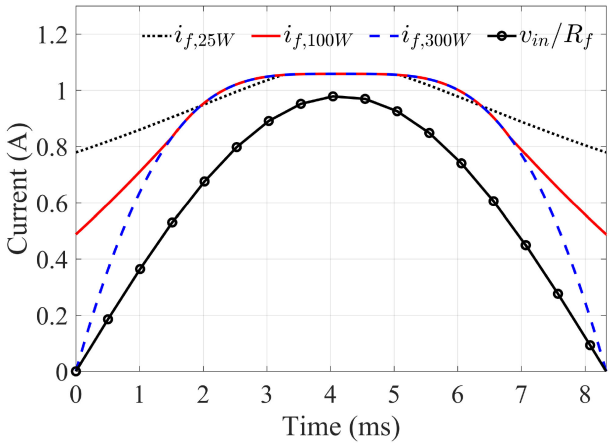

Fig. 9. Fictitious current of LEM-OCC-SD, during half of a line cycle, for different input powers. $V_{\text{in}}^{\text{rms}} = 250$ V, $R_f = 361\,\Omega$.

Considering the parameters given in Table II, the fictitious current of LEM-OCC-SD is calculated for different power levels. The results are shown in Fig. 9. $R_f = 361\,\Omega$ is calculated to achieve stability down to no-load operation.

C. Leading-Edge Modulated One-Cycle Control-SDS

Generating the fictitious current from (33) and (34) requires a digital controller or complex analog circuits, so it is desirable to have a simpler solution to implement an approximation of i_f. Different approximations can be made depending on the desired complexity of the resulting application circuit. Inspired by the fictitious current waveforms in Fig. 9, obtained by simulating the converter of Table II controlled by LEM-OCC-SD, the proposed approximation is

$$i_f = a - bP^* = (a - bP^*)\left(|\sin(\omega t)| + (1 - |\sin(\omega t)|)\right) \quad (39)$$

with $i_f > 0$, a and b constants to be determined, and P^* the output of the output voltage controller, given by

$$P^* = \frac{(V_{\text{in}}^{\text{rms}})^2}{R_e} \quad (40)$$

which is considered a constant value in steady state.

It is clear that for low P^* (i.e., low input power), (39) results in $i_f \to a$, which is a constant value similar to $i_{f,25\,W}$ in Fig. 9. However, for high input power in (39), $i_f \to 0$, which is not similar to $i_{f,300\,W}$. This is possible because the stability term $|v_{\text{in}}|/R_f$ is the predominant term when input power is high, and since LEM-OCC can be naturally stable in this condition, i_f can be set to zero to simplify the resulting control circuit.

This is further clarified by separating (39) into two terms, one for guaranteeing stability, given by

$$i_f^s = (a - bP^*)\,|\sin(\omega t)| \to \frac{1}{R_f} = \frac{a - bP^*}{\sqrt{2}V_{\text{in}}^{\text{rms}}} \quad (41)$$

and one term for improving THD in both CCM and DCM

$$i_f^e = (a - bP^*)(1 - |\sin(\omega t)|) \quad (42)$$

where $\omega = 2\pi f_r$ is the angular frequency of the input voltage.

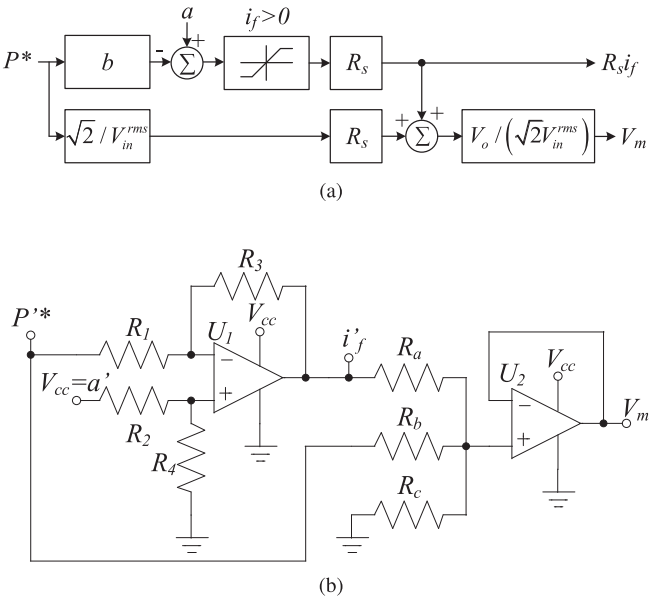

Fig. 10. LEM-OCC-SDS. (a) Block diagram. (b) Analog implementation circuit.

This approximation is used for both CCM and DCM operation, and it does not require conduction mode detection. The resulting control strategy is referenced here as LEM-OCC-SDS.

To guarantee stability, the domain of $\{a, b\}$ should be restricted by (32), which is combined with (1), (40), and (41) to yield the form

$$a - bP^* \geq \sqrt{2}V_{\text{in}}^{\text{rms}} \left(\frac{2\sqrt{2}V_{\text{in}}^{\text{rms}} - V_o}{2L_B f_s V_o} - \frac{P^*}{\left(V_{\text{in}}^{\text{rms}}\right)^2} \right). \quad (43)$$

Since R_f now varies with the input power, V_m is rewritten as a function of P^* by combining (31), (40), yielding

$$V_m = \frac{V_o R_s}{\sqrt{2}V_{\text{in}}^{\text{rms}}} \left(\frac{\sqrt{2}P^*}{V_{\text{in}}^{\text{rms}}} + a - bP^* \right). \quad (44)$$

The block diagram to implement the proposed fictitious current is shown in Fig. 10(a) and uses only summers, amplifiers, and limiters, which are simple to implement with an analog hardware. This block diagram implements the proposed simplification without sensing the input voltage and, therefore, the value of $V_{\text{in}}^{\text{rms,max}}$ is used. Since $V_{\text{in}}^{\text{rms,max}}$ is the worst condition for LEM-OCC, the block diagram still fulfills the stability criterion for the whole operating range of the converter. Without input voltage feedforward, P^* will only be close to P_{in} when the real input voltage is the same as the value used in the block diagram.

A circuit for an analog implementation of the block diagram shown in Fig. 10(a) is depicted in Fig. 10(b). The circuit outputs V_m directly to the OCC integrator. The remaining analog signals are normalized to the available V_{cc} range to decrease the effects of offsets and noise in the circuit. The summer to implement $R_s(i_f + i_{DB})$ should properly account for these normalized values. Normalized signals are identified by the $'$ symbol. Since the maximum value of i_f in (39) is a, a is mapped to V_{cc}, such that

$$a' = V_{cc} = a\frac{V_{cc}}{a} \quad (45)$$

$$i'_f = i_f \frac{V_{cc}}{a}. \quad (46)$$

The normalization of P^* should consider that at low input voltage $P^* \gg P_{\text{in}}^{\max}$ due to the lack of input voltage feedforward, that is

$$P'^* = V_{cc}\frac{P^*}{P^*_{\text{norm}}} \quad (47)$$

where the normalization value P^*_{norm} can be evaluated by simulating the converter with LEM-OCC-SDS at the operating point with minimum input voltage and maximum output power. The limiter $i_f > 0$ is implemented without additional hardware by using single supply operational amplifiers.

The resistor values for the proposed analog circuit should be calculated to realize the gains in (48) and (49). Equations (48) and (49) are obtained by applying the normalized values to the block diagram in Fig. 10(a) and, then, comparing to the circuit equations of the analog circuit. Operational amplifier U_1 in Fig. 10(b) implements

$$i'_f = a' - P'^* b\frac{P^*_{\text{norm}}}{a} = a'\frac{R_4}{R_2+R_4}\frac{R_1+R_3}{R_1} - P'^*\frac{R_3}{R_1} \quad (48)$$

and operational amplifier U_2 implements

$$\begin{aligned} V_m &= i'_f \frac{aR_s V_o}{V_{cc}\sqrt{2}V_{\text{in}}^{\text{rms,max}}} + P'^* \frac{R_s P^*_{\text{norm}} V_o}{V_{cc}\left(V_{\text{in}}^{\text{rms,max}}\right)^2} \\ &= i'_f \frac{R_b||R_c}{R_a + R_b||R_c} + P'^* \frac{R_a||R_c}{R_b + R_a||R_c} \end{aligned} \quad (49)$$

where symbol $||$ represents the parallel equivalent product of two resistors.

Optimal values of a and b should be found to improve the input current THD for given application requirements. By using LEM-OCC-SDS, the THD of the input current is a function of the parameters a and b, the input power P_{in} and the input voltage $V_{\text{in}}^{\text{rms}}$, that is

$$\text{THD}(a, b, P_{\text{in}}, V_{\text{in}}^{\text{rms}}). \quad (50)$$

One option to obtain adequate values for a and b is to simulate the converter for different pairs of $\{a, b\}$, to plot the THD as a function of the input power, such as done in Fig. 3, and to choose one adequate set to the application. The comparison can be performed only at maximum input voltage $V_{\text{in}}^{\text{rms,max}}$ since this is the worst condition for LEM-OCC.

However, it is desirable to have a consistent way to compare the performance of distinct pairs $\{a, b\}$, without relying on waveforms. This can be done by calculating the average input current THD, THD_{avg}, in the input power range, $P_{\text{in}}^{\min}$ to $P_{\text{in}}^{\max}$, of the converter, that is

$$\begin{aligned} &\text{THD}_{\text{avg}}(a, b) \\ &\quad = \frac{1}{P_{\text{in}}^{\max} - P_{\text{in}}^{\min}} \int_{P_{\text{in}}^{\min}}^{P_{\text{in}}^{\max}} \text{THD}(a, b, P_{\text{in}}, V_{\text{in}}^{\text{rms,max}}) \text{d}P_{\text{in}}. \end{aligned} \quad (51)$$

It is also possible to use the weighted average of the input current THD, THD_{wavg}, to allow optimizing the THD at specific power levels

$$\text{THD}_{\text{wavg}}(a,b) = \frac{1}{P_{\text{in}}^{\max}-P_{\text{in}}^{\min}}\int_{P_{\text{in}}^{\min}}^{P_{\text{in}}^{\max}} W_P(P_{\text{in}})\cdot \text{THD}(a,b,P_{\text{in}},V_{\text{in}}^{\text{rms}})\text{d}P_{\text{in}} \tag{52}$$

where $W_P(P_{\text{in}})$ is the weighting factor when input power is P_{in} and

$$\int_{P_{\text{in}}^{\min}}^{P_{\text{in}}^{\max}} W_P(P_{\text{in}})\text{d}P_{\text{in}} = 1. \tag{53}$$

The weighted average is a consistent way of comparing each set $\{a,b\}$, used for generating the fictitious current. It can be calculated from simulation results or analytically, by solving (15) and (22) over a line period.

Lower values of THD_{wavg} indicate that the set $\{a,b\}$ has a lower overall THD, especially at the input powers where $W_P(P_{\text{in}})$ is higher. Additionally, $\text{THD}_{\text{wavg}} := \infty$ if $\{a,b\}$ does not satisfy the stability criterion (43). The weighting factor $W_P(P_{\text{in}})$ can be determined from application requirements or normative standards. However, if the required normative standard only evaluates harmonics at rated power, the simple average from (51) would be adequate.

It is possible to solve (52) numerically for different sets $\{a,b\}$ to find a set that results in the lowest THD_{wavg}. To limit the number of sets $\{a,b\}$ that should be evaluated, the evaluated sets can be centered around initial values obtained by comparing the two sides of (43)

$$a_{\text{init}} = \sqrt{2}V_{\text{in}}^{\text{rms}}\frac{2\sqrt{2}V_{\text{in}}^{\text{rms}}-V_o}{2L_Bf_sV_o} \tag{54}$$

$$b_{\text{init}} = \frac{\sqrt{2}V_{\text{in}}^{\text{rms}}}{(V_{\text{in}}^{\text{rms}})^2}. \tag{55}$$

The converter of Table II is simulated at different operating points with both LEM-OCC-SD and LEM-OCC-SDS control strategies. The resulting average input current waveforms are presented in Fig. 11. LEM-OCC-SD has almost no distortion while LEM-OCC-SDS can decrease the average value of the input current error but cannot fully compensate for it.

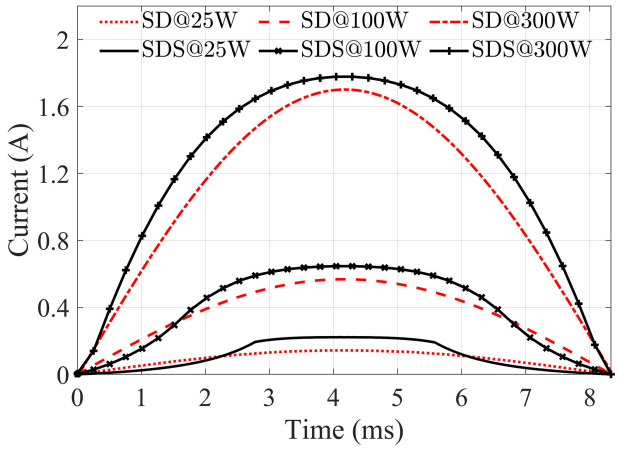

Fig. 11. Average input current of LEM-OCC-SD and LEM-OCC-SDS for different values of P^*. $V_{\text{in}}^{\text{rms}} = 250$ V. $R_f = 361\,\Omega$ for LEM-OCC-SD. $a = 0.978$ and $b = 0.0028$ for LEM-OCC-SDS.

TABLE III
COMPONENTS OF TPBR PROTOTYPE

Component	Description
S_1, S_2	STGB20V60F
D_1, D_2	VS-15AW-L06FN
D_{B1}, D_{B2}	C4D05120E
C_o	EKMM401VSN271MA30S
L_B	Powder Core - 3.2 mH@1 A, 2.4 mH@5 A
DSP	TMS320F28377S

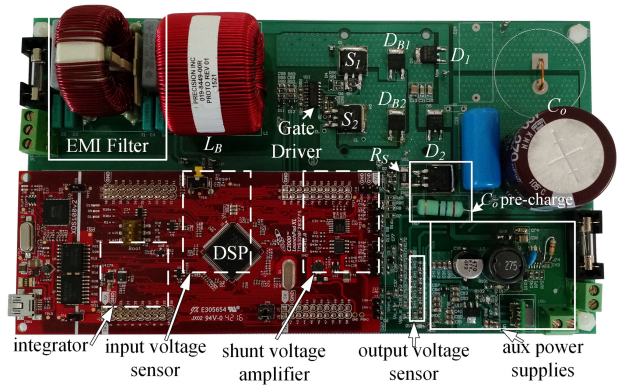

Fig. 12. 300 W TPBR prototype using a shunt current sensor.

V. EXPERIMENTAL RESULTS

A TPBR with the specifications shown in Table II and components listed in Table III was built for experimental validation of the proposed control strategies. A picture of the prototype is shown in Fig. 12 and the overall control structure considering the implementation of LEM-OCC-SD is presented in Fig. 13. For LEM-OCC-SD, the fictitious current generation involves solving (38) to decide if the DCM or CCM equation of the fictitious current should be used. The fictitious current is then calculated from (28) and (33) for CCM or from (34) for DCM. The implementation of LEM-OCC-SDS is based on the block diagram of Fig. 10(a) and differs from Fig. 13 by the different fictitious current and V_m generation. Shunt resistor R_{SH} and an amplifier with gain G_{RS} are used for current sensing, resulting in the equivalent sensing resistance $R_s = R_{SH}G_{RS}$.

The DSP to implement LEM-OCC-SD requires two analog-to-digital converters (ADC), two digital-to-analog converters (DAC) and a PWM module that can accept an external reset trigger. LEM-OCC-SD also requires one analog summer, one comparator, and one integrator. The fictitious current is a low-frequency signal, as can be seen in Fig. 9, and V_m is almost constant. Therefore, a low-cost DSP with a PWM module and an analog filter to implement the DAC would achieve enough bandwidth and resolution. The maximum value of i_f is relatively small compared to the maximum input current, so it is useful to normalize the DAC output instead of directly using $R_s i_f$.

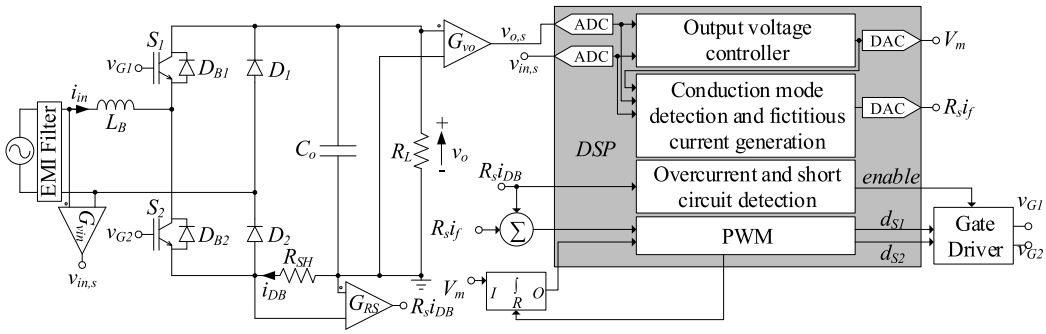

Fig. 13. Implementation of LEM-OCC-SD.

This allows proper use of all the resolution of the DAC. For the fictitious current in Fig. 9, a normalized output of an 8-bit DAC allows for 4.3 mA of resolution, which represents 3% of the peak input current at minimum load with maximum input voltage. To simplify the external circuits, the chosen DSP has a PWM module with internal analog comparators, but an external analog summer and integrator are required. Two 12-bit ADC and two 12-bit DAC converters are used. Although some of the LEM variations could be implemented analogically as mentioned before, all three options were digitally programmed. The generation of the fictitious currents and the decision on the operation modes are part of the DSP software structure as depicted in Fig. 13. For LEM-OCC-SD, it is used $R_f = 320\,\Omega$, which is higher than the required at no-load to give stability margin. For LEM-OCC-SDS, $a = 1.04$ and $b = 0.00305$ were computed to minimize (51).

When operating in DCM with low input currents, the voltage rising time of the switches is increased as parasitic capacitances take longer to charge [27], increasing the effective duty ratio. With the proposed control structure, the nonoperating switch receives a gating signal when the operating switch turns OFF (with appropriate deadtime specified in the gate driver to avoid shoot through). This leads to a duty ratio closer to the desired value, as the parasitic capacitances can be charged with current from the output capacitor. The use of GaN semiconductors has the potential to get duty ratio closer to the desired value and is a possible future work.

The maximum duty ratio is limited at 0.95 giving 772 ns for current sensing to settle down. The fictitious current is calculated using $L_B = 3.2$ mH, prioritizing compensation at low input current, since the inductance of the chosen inductor drops to 2.4 mH at its maximum current. A digital moving average filter is used for minimizing the effect of output voltage ripple in the input current THD. Input voltage feedforward is also realized using a sliding window root mean square (rms) computation. The output voltage control loop and fictitious current generation use a 5.4 kHz sampling rate, while the switching frequency is 64.8 kHz. The control loop execution takes 3.63 μs for LEM-OCC-SD, including calculation of output voltage moving average filter, output voltage control, input voltage feedforward, and fictitious current. This represents 23% of a switching period and only 2% of total CPU usage due to the 5.4 kHz control loop execution rate. The fictitious current alone takes 282 ns to update for LEM-OCC-SD. LEM-OCC-SDS decreases total execution time to 3.13 μs, as it has simpler fictitious current and V_m calculations and lacks input voltage feedforward.

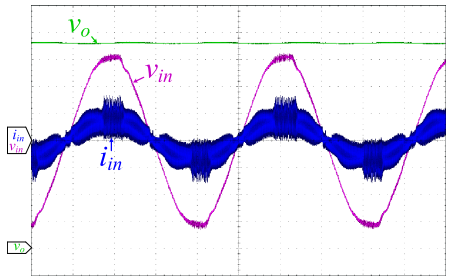

Fig. 14. Instability of LEM-OCC at high emulated resistance. $V_{\text{in}}^{\text{rms}} = 220$ V and $P_{\text{in}} = 58.4$ W.

The converter is initially operated with the conventional LEM-OCC with a 50 W load. Instability is verified at the positive and negative input voltage peaks, as can be observed in Fig. 14.

Experimental results comparing the three extensions discussed in this article are presented in Figs. 15, 16, and 17, for distinct input voltages and power levels.

Fig. 15 presents the operation with minimum load and input voltage. In Fig. 15(a), LEM-OCC-S has significant distortion around zero crossing. The converter operates with a maximum duty ratio close to zero crossing resulting in overshoot of the input current. This occurs due to poor signal to noise ratio and voltage offset of the sensors. This effect is not as noticeable in LEM-OCC-SD in Fig. 15(b) and LEM-OCC-SDS in Fig. 15(c), as in these strategies i_f^e is not zero around zero crossing, improving the signal to noise ratio at the comparator and minimizing the effect of offsets in the signals.

Fig. 16 presents the operation with minimum load and maximum voltage, which is the worst condition for LEM-OCC. In Fig. 16(a), LEM-OCC-S is seen to have significant current distortion, with THD of 75% and spikes in zero crossing are still visible. LEM-OCC-SD, in Fig. 16(b), has the best performance in this case, with THD around 13%, while LEM-OCC-SDS, in Fig. 16(c), has THD around 30%.

For high input power, the compensation has little effect, as the converter operates in CCM with low current ripple. Experimental results of LEM-OCC-SD at maximum input power and maximum input voltage are shown in Fig. 17.

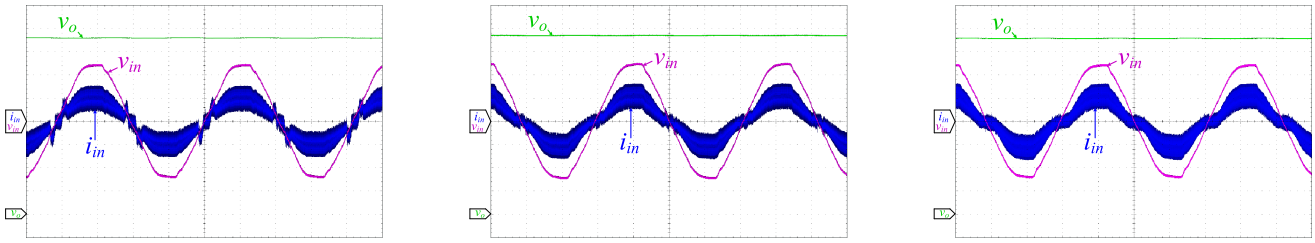

Fig. 15. Experimental results: 25W@85 V. Time: 4 ms/div, v_o: 50 V/div, v_{in}: 50 V/div, i_{in}: 500 mA/div. (a) LEM-OCC-S. (b) LEM-OCC-SD. (c) LEM-OCC-SDS.

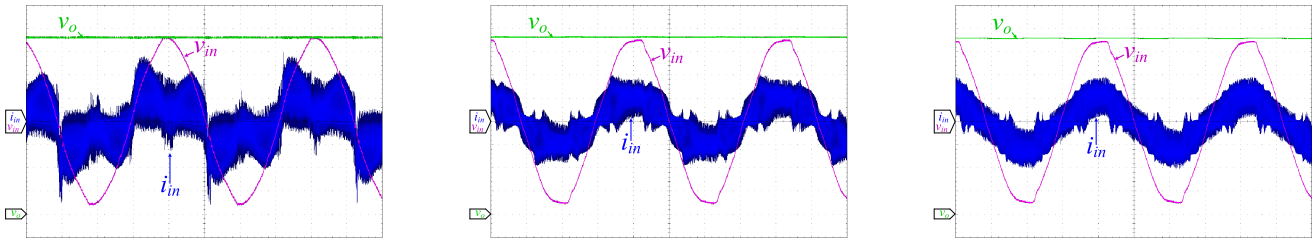

Fig. 16. Experimental results: 25W@250 V. Time: 4 ms/div, v_o: 50 V/div, v_{in}: 100 V/div, i_{in}: 200 mA/div. (a) LEM-OCC-S. (b) LEM-OCC-SD. (c) LEM-OCC-SDS.

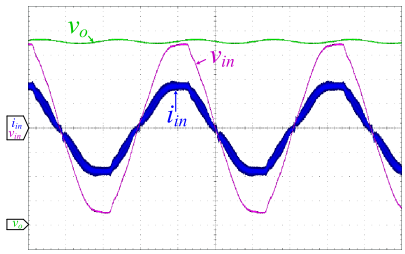

Fig. 17. Experimental results of LEM-OCC-SD: 300W@250 V. Time: 4 ms/div, v_o: 50 V/div, v_{in}: 100 V/div, i_{in}: 1 A/div.

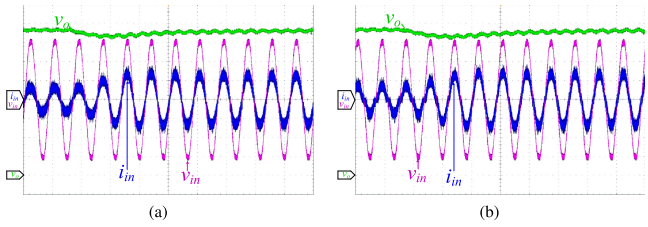

Fig. 18. Experimental results of load step with $P_{\text{in}} = 110$ W$\rightarrow P_{\text{in}} = 210$ W. $V_{\text{in}}^{\text{rms}} = 220$ V. Time: 4 ms/div, v_o: 50 V/div, v_{in}: 100 V/div, i_{in}: 1 A/div. (a) LEM-OCC-SD. $\Delta V_o = -15\ V$. (b) LEM-OCC-SDS. $\Delta V_o = -17\ V$.

A load step which brings P_{in} from 110 to 210 W is applied to the converter operating with both OCC extensions as depicted in Fig. 18. There is no instability in current control during these steps, as expected from the stability analysis.

An input voltage step, from 110 to 220 V is also applied to the converter operating with LEM-OCC-SD as depicted in Fig. 19. When using LEM-OCC-SDS, the output voltage controller has worse transient response due to the lack of input voltage feedforward, and the output overvoltage protection (OVP) is tripped,

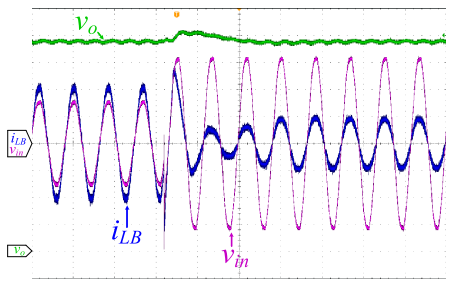

Fig. 19. Experimental results of LEM-OCC-SD during input voltage step from $V_{\text{in}}^{\text{rms}} = 110$ V$\rightarrow V_{\text{in}}^{\text{rms}} = 220$ V. $P_{\text{in}} = 300$ W. Time: 20 ms/div, v_o: 50 V/div, v_{in}: 100 V/div, i_{in}: 2 A/div. $\Delta V_o = 41\ V$.

turning OFF the converter. An OVP with autorestart needs to be implemented for the converter to operate during such voltage transients.

For the target application of household refrigerators, the normative energy quality requirements are Class D of IEC 61000-3-2 [28] and JIS C 61000-3-2 [29]. All three control solutions based on LEM-OCC can meet these requirements because the input current harmonics are evaluated at rated power, when THD is low. However, it is still desirable to have low THD at light load because the application is for refrigerators. The THD content is related to the input power variation in Fig. 20 for two distinct input voltage values. LEM-OCC-SD and LEM-OCC-SDS do not show a significant advantage at low input voltage but have a very clear advantage when operating with maximum input voltage.

A comparison between the simulation results in Fig. 3 and the experimental results in Fig. 20 shows that the close-to-zero THD achieved by LEM-OCC-SD in simulation is not reached in practice. LEM-OCC-SDS also has worse performance in practice than in simulation. This difference results from effects that

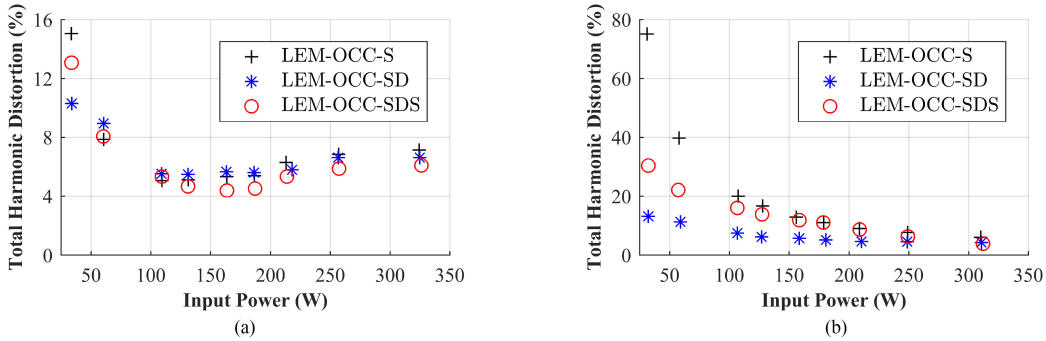

Fig. 20. Experimental results of input current THD. (a) $V_{\text{in}}^{\text{rms}} = 85$ V. (b) $V_{\text{in}}^{\text{rms}} = 250$ V.

TABLE IV
ESTIMATED COST OF BLOCKS OF THE CONTROL SYSTEM OF A TPBR USING DIFFERENT IMPLEMENTATIONS

Control Strategy	Cost breakdown (US$)			
	Control Logic	Input Current Sensor	Input Voltage Sensor	Total
Digital-Average	4.269	2.552	0.352	7.173
TEM-OCC	1.285	2.552	0.272	4.109
LEM-OCC-SD	5.401	0.641	0.352	6.394
LEM-OCC-SDS (Analog, Discrete)	2.707	0.641	0.272	3.620
LEM-OCC-SDS (Analog, Integrated)	1.285	0.124	0.272	1.681

are not included in the model used for calculating the fictitious current, such as inductance variation with input current, duty ratio distortion due to dead-time of the switches, effect of the *LC* resonance between input inductor and parasitic capacitances, grid impedance and offsets in the control circuits. However, the overall trend expected from the simulation is verified, with LEM-OCC-SD achieving the lowest THD and LEM-OCC-SDS having lower performance, but still significantly improving over LEM-OCC.

The comparison of the experimental results with the simulation results also show that LEM-OCC-SD can achieve performance similar to A-A control. The tradeoff is that LEM-OCC-SD requires a DSP while A-A control requires a more expensive sensor. A low-cost DSP can be used since the fictitious current update rate is low compared to the switching frequency and total CPU usage was verified to be low in the experiments. The DSP also has potential to bring additional functionality to the application. On the other hand, LEM-OCC-SDS is very competitive with TEM-OCC, since they have similar performance, neither requires a DSP or input voltage waveform sensing, but LEM-OCC-SDS has the advantage of using a simpler current sensor.

A cost estimate of the bill of materials (BOM) of the control circuits was performed to verify the feasibility of the proposed control scheme. The results are shown in Table IV. TEM-OCC is verified as the lower cost alternative in the current market. However, LEM-OCC-SD has spare processing time and unused pins in the DSP, allowing implementation of other system functionalities at lower cost. LEM-OCC-SD requires more analog circuits than D-A control, but it still reaches a lower price due to the lower cost of the shunt resistor. An implementation of LEM-OCC-SDS using discrete analog components is not a viable alternative, since the cost difference is compensated by the lack of some features such as OVP. An implementation of LEM-OCC-SDS in an integrated circuit is an attractive solution, which can reach a BOM cost reduction of up to 59% when compared to TEM-OCC.

VI. CONCLUSION

LEM-OCC is an interesting control strategy that requires only a shunt resistor for current sensing in the TPBR. However, it can be unstable at light load with high input voltage and presents high input current distortion. This article has proposed two extensions to LEM-OCC to solve this issue. Compared to previously proposed variations of OCC, these new proposals achieve both stability and low input current THD over the full input power and input voltage ranges of the converter, even when operating in DCM. The better performing strategy, LEM-OCC-SD, requires a DSP. A simplified strategy, LEM-OCC-SDS, has lower performance but can be implemented analogically.

A prototype with 300 W output power for input voltages of 85 to 250 V was built. LEM-OCC without the proposed extensions was verified as unstable in the experiments. The use of a well-known extension resulted in input current THD of 75% for 10% load at maximum input voltage. At the same operating conditions, LEM-OCC-SD achieved THD of around 13% and LEM-OCC-SDS achieved THD of around 30%.

Possible future works include the application to other power topologies, study of the effect of faster switches on current sensing, analyzing the stability and performance of the controller when considering the electromagnetic interference filter, grid impedance and varying boost inductance in a line cycle due to permeability change.

REFERENCES

[1] J. C. Salmon, "Circuit topologies for PWM boost rectifiers operated from 1-phase and 3-phase ac supplies and using either single or split dc rail voltage outputs," in *Proc. 10th Annu. Appl. Power Electron. Conf. Expo.*, Mar. 1995, vol. 1, pp. 473–479.

[2] L. Huber, Y. Jang, and M. M. Jovanovic, "Performance evaluation of bridgeless PFC boost rectifiers," *IEEE Trans. Power Electron.*, vol. 23, no. 3, pp. 1381–1390, May 2008.

[3] W. Wu, "1.5 kW digital totem pole PFC design for air-conditioner and performance comparison using IGBT, SiC and GaN," in *Proc. PCIM Europe Int. Exhib. Conf. for Power Electron., Intell. Motion, Renewable Energy Energy Manag.*, May 2017, pp. 1–5.
[4] L. Zhou, Y. Wu, J. Honea, and Z. Wang, "High-efficiency true bridgeless totem pole PFC based on GaN HEMT: Design challenges and cost-effective solution," in *Proc. PCIM Europe Int. Exhib. Conf. for Power Electron., Intell. Motion, Renewable Energy Energy Manag.*, May 2015, pp. 1–8.
[5] B. Zhang, K. Shi, Q. Lin, G. M. Dousoky, M. Shoyama, and S. Tomioka, "Conducted noise reduction of totem-pole bridgeless PFC converter using GaN HEMTs," in *Proc. IEEE Int. Telecommun. Energy Conf.*, Oct. 2015, pp. 1–5.
[6] K. M. Smedley and S. Cuk, "One-cycle control of switching converters," *IEEE Trans. Power Electron.*, vol. 10, no. 6, pp. 625–633, Nov. 1995.
[7] Z. Lai and K. M. Smedley, "A family of continuous-conduction-mode power-factor-correction controllers based on the general pulse-width modulator," *IEEE Trans. Power Electron.*, vol. 13, no. 3, pp. 501–510, May 1998.
[8] C. Qiao, K. M. Smedley, Z. Lai, and M. Nabant, "An improved integration-reset controlled single phase unity-power-factor boost rectifier with lower distortion," in *Proc. Conf. Proc. 25th Annu. Conf. IEEE Ind. Electron. Soc.*, Nov. 1999, vol. 1, pp. 272–277.
[9] D. V. Ghodke, B. G. Fernandes, and K. Chatterjee, "PLL-less one cycle controlled bi-directional high power factor AC to DC converter," in *Proc. PESC Rec.—IEEE Annu. Power Electron. Spec. Conf.*, 2006, pp. 1–6.
[10] Z. Lai and K. M. Smedley, "A new extension of one-cycle control and its application to switching power amplifiers," *IEEE Trans. Power Electron.*, vol. 11, no. 1, pp. 99–105, Jan. 1996.
[11] Y. Chen and K. M. Smedley, "A cost-effective single-stage inverter with maximum power point tracking," *IEEE Trans. Power Electron.*, vol. 19, no. 5, pp. 1289–1294, Sep. 2004.
[12] D. Yang, M. Yang, and X. Ruan, "One-cycle control for a double-input dc/dc converter," *IEEE Trans. Power Electron.*, vol. 27, no. 11, pp. 4646–4655, Nov. 2012.
[13] L. Zhang, X. Ruan, and X. Ren, "One-cycle control for electrolytic capacitor-less second harmonic current compensator," *IEEE Trans. Power Electron.*, vol. 33, no. 2, pp. 1724–1739, Feb. 2018.
[14] K. M. Smedley, L. Zhou, and C. Qiao, "Unified constant-frequency integration control of active power filters-steady-state and dynamics," *IEEE Trans. Power Electron.*, vol. 16, no. 3, pp. 428–436, May 2001.
[15] K. Chatterjee, A. Chandra, K. Al-Haddad, and P. J. Lagace, "A PLL less VAr generator based on one-cycle control," in *Proc. 11th Int. Conf. Harmonics Quality Power*, Sep. 2004, pp. 512–518.
[16] K. Chatterjee, A. Chandra, and K. Al-Haddad, "PLL-less one-cycle controlled modified load compensator for wide range of loads," in *Proc. PESC Rec—IEEE Annu. Power Electron. Spec. Conf.*, 2005, pp. 2322–2326, vol. 2005.
[17] T. Jiang, P. Mao, and S. Xie, "Analysis and improvement on input current of one-cycle controlled PFC converter," in *Proc. 5th IEEE Conf. Ind. Electron. Appl.*, Jun. 2010, pp. 2094–2098.
[18] N. Vamanan and V. John, "Dual comparison one cycle control for single phase ac to dc converters," *IEEE Trans. Ind. Appl.*, vol. 52, no. 4, pp. 3267–3278, Jul. 2016.
[19] N. Vamanan and V. John, "Dual-comparison one-cycle control for single-phase bidirectional power converters," *IEEE Trans. Ind. Appl.*, vol. 54, no. 5, pp. 4621–4631, Sep. 2018.
[20] P. C. Todd, "UC3854 controlled power factor correction circuit design," *Unitrode Application Note U-134*, pp. 3–269, 3–288.
[21] S. Buso, P. Mattavelli, L. Rossetto, and G. Spiazzi, "Simple digital control improving dynamic performance of power factor preregulators," *IEEE Trans. Power Electron.*, vol. 13, no. 5, pp. 814–823, Sep. 1998.
[22] R. Brown and M. Soldano, "One cycle control IC simplifies PFC designs," in *Proc. 20th Annu. IEEE Appl. Power Electron. Conf. Expo.*, Mar. 2005, vol. 2, pp. 825–829.
[23] D. M. V. de Sype, K. D. Gusseme, A. P. V. den Bossche, and J. A. A. Melkebeek, "A sampling algorithm for digitally controlled boost PFC converters," *IEEE Trans. Power Electron.*, vol. 19, no. 3, pp. 649–657, May 2004.
[24] B. Lu, R. Brown, and M. Soldano, "Bridgeless PFC implementation using one cycle control technique," in *Proc. 20th Annu. IEEE Appl. Power Electron. Conf. Expo.*, Mar. 2005, vol. 2, pp. 812–817.
[25] F. C. Moon, *Chaotic Vibrations-An Introduction for Applied Scientists and Engineers*. New York, NY, USA: Wiley, 1987.
[26] K. D. Gusseme, D. M. V. de Sype, A. P. M. V. den Bossche, and J. A. Melkebeek, "Digitally controlled boost power-factor-correction converters operating in both continuous and discontinuous conduction mode," *IEEE Trans. Ind. Electron.*, vol. 52, no. 1, pp. 88–97, Feb. 2005.
[27] K. Upamanyu, D. Venkatramanan, A. Adapa, and G. Narayanan, "Experimental study on the influence of dead-time on IGBT turn-off characteristics in an inverter leg at high and low currents," in *Proc. 7th India Int. Conf. Power Electron.*, Nov. 2016, pp. 1–5.
[28] "Electromagnetic compatibility (EMC) - Part 3-2: Limits - Limits for harmonic current emissions (equipment input current <=16 A per phase)," International Electrotechnical Commission, Geneva, Switzerland, Standard, 2018.
[29] "Electromagnetic compatibility (EMC) Part 3-2: Limits - Limits for harmonic current emissions (equipment input current <=20 A per phase)," Japanese Standards Association, Tokyo, Japan, Standard, 2011.

Guilherme da Silva Fischer received the B.S. and M.S. degrees in electrical engineering from Santa Catarina State University, Joinville, Brazil, in 2016 and 2018, respectively.

His research interests include modeling and control of static converters.

Cassiano Rech (S'01–M'06–SM'15) received the B.S., M.S., and Ph.D. degrees in electrical engineering from the Federal University of Santa Maria (UFSM), Santa Maria, Brazil, in 1999, 2001, and 2005, respectively.

From 2005 to 2007, he was with the Universidade Regional do Noroeste do Estado do Rio Grande do Sul. From 2008 to 2009, he was with Santa Catarina State University. Since 2009, he has been with the UFSM, where he is currently a Professor. His research interests include multilevel converters, distributed generation, and modeling and digital control techniques applied to static converters.

Dr. Rech was the Editor-in-Chief of the *Brazilian Power Electronics Journal* from 2014 to 2015. From 2016 to 2017, he was the President of the Brazilian Power Electronics Society. Since 2018, he has been an Associate Editor of the IEEE TRANSACTIONS ON INDUSTRIAL ELECTRONICS.

Yales Rômulo de Novaes (M'04) was born in Indaial, Santa Catarina, Brazil, in 1974. In 1999, he received the B.S. degree in electrical engineering from the FURB—Regional University of Blumenau, Santa Catarina, Brazil. He received the M. Eng. and doctorate degrees from the Power Electronics Institute (INEP) of the Federal University of Santa Catarina, Florianópolis, Brazil, in 2000 and 2006, respectively.

During 2001, he was a Researcher Engineer with INEP. From 2006 to 2008, he was a Postdoctoral Fellow with the Industrial Electronics Laboratory at École Polytechnique Fédérale de Lausanne, Lausanne, Switzerland. From 2008 to 2010, he was a Scientist with Power Electronics Systems Group, ABB Corporate Research Center, Daetwill, Switzerland. He is currently an Associate Professor with Santa Catarina State University, Joinville, Brazil and, Coordinator of Research Cell on Microgrids of Alternative and Renewable Energies.